Materials Horizons

ROYAL SOCIETY OF CHEMISTRY

COMMUNICATION

View Article Online
View Journal

Cite this: DOI: 10.1039/d5mh01287b

Received 24th July 2025,
Accepted 17th October 2025

DOI: 10.1039/d5mh01287b

rsc.li/materials-horizons

In situ nanoscale heterostructure engineering for additive manufacturing of dynamic adaptive alloys

Junchao Yi [a] and Gary J. Cheng *[ab]

Achieving precision and balanced properties in additive manufacturing (AM) of metallic alloys remains challenging due to rapid melting–solidification cycles, leading to unpredictable microstructures and inconsistent mechanical performance. Conventional AM suffers from high costs, limited adaptability, and brittle secondary phases, compromising load-bearing capacity and structural precision, particularly in alloys like nickel-titanium (NiTi) that are sensitive to high-energy inputs. To overcome these limitations, we present an *in situ* nanoscale heterostructure engineering (INSHE) strategy that addresses the trade-offs in AM for achieving enhanced mechanical and functional properties. INSHE leverages high-energy laser powder bed fusion (L-PBF) to create uniformly distributed multi-nanoprecipitate assemblies with lattice-matched interfaces, achieving precise modulation of non-equilibrium microstructures from the bottom up. By controlling the inclusion of multi-precipitate seeds and ultrafine heterostructures, INSHE maintains thermodynamic stability under L-PBF's extreme conditions, achieving consistent distribution across the build direction. When applied to a NiTi shape memory alloy, INSHE formulates boron carbide (B_4C) additively to form a nanoengineered B2-TiB_2-TiC phase heterostructure that enhances both strength and adaptability beyond conventional alloys. INSHE-based shape memory alloys (SMAs) demonstrate an ultrahigh yield strength of up to 2.15 GPa with a delayed plasticity of 12%, more than double the hardness of pristine SMAs (4.94 GPa), and a 66% increase in the hardness-to-modulus ratio (H/E_r), which promotes wear resistance *via* lubricating oxide film formation. INSHE-engineered SMA mechanical metamaterials (SMMMs) demonstrate superior strain recovery and durability under cyclic and gradient loads over conventional SMAs. These SMMMs achieve specific energy absorption (SEA) up to 25 J g^{-1}, surpassing the typical 1–20 J g^{-1} range of composites and other micro-/nanolattice metals, demonstrating exceptional resilience. The activation of corresponding variant pairs (CVPs)—twin-related martensitic variants—enhances cyclic phase transformations, prevents stabilized martensite retention, and enables efficient energy absorption.

New concepts

We introduce an *in situ* nanoscale heterostructure engineering (INSHE) strategy as a breakthrough in alloy design for additive manufacturing (AM), enabling simultaneous enhancement of printability, structural fidelity, and functional performance. Unlike conventional approaches that rely on equilibrium-phase alloy chemistries or post-processing to introduce functional phases, INSHE leverages laser-driven thermochemical reactions and lattice-matched nanoscale assembly to create uniform dual-nanoprecipitates directly during printing. This strategy enables real-time microstructure modulation across multiple scales, unlocking bottom-up control of alloy behavior and eliminating long-standing trade-offs between strength, ductility, and print precision. Unlike prior works that incorporate passive nanoparticles or metastable additives into feedstock, INSHE actively triggers nanometallurgical transformations *in situ*, improving thermal stability, increasing laser absorptivity, and achieving high-fidelity 3D structures with smooth surfaces. The resulting adaptive alloys exhibit exceptional mechanical and damping properties—surpassing leading AM alloys in specific energy absorption, fatigue resistance, and phase transformation dynamics—without the need for post-treatment. INSHE represents a paradigm shift in AM alloy design, introducing a dynamic material platform where the microstructure, mechanical performance, and functionality are co-optimized through process-informed design. This concept paves the way for high-performance adaptive materials for advanced applications in sensing, energy harvesting, aerospace, and biomedical devices.

INSHE's nanoengineered heterostructure within the B2 phase promotes multiple synergistic deformation mechanisms that resist shear-induced amorphization and prevent crystalline fragmentation. This results in significantly improved damping capacity, linear elastic behavior across transformation temperatures, and nearly ideal shape recovery, achieving superior actuation efficiency over multicomponent and commercial Snoek-type high-damping alloys. Micro-CT imaging confirms INSHE's superior internal quality and precision in complex geometries, addressing powder adhesion and surface roughness through enhanced powder absorption and thermochemical tuning. INSHE also advances printability by refining powder feedstock design and laser processing parameters. This transformative strategy paves the way for the application of alloys with tailored multifunctional properties in topological architectures, unlocking new possibilities for dynamic adaptive materials with superior structural and functional performance.

[a] *The Institute of Technological Sciences, Wuhan University, Wuhan 430072, P. R. China. E-mail: gjcheng@purdue.edu*
[b] *School of Industrial Engineering, Purdue University, West Lafayette, IN 47906, USA*

Introduction

Additive manufacturing, also known as three-dimensional (3D) printing, is disrupting the energy-intensive production paradigm in engineering and technology that has long separated the making, shaping, and treating processes of material components.[1,2] However, the multiple physical and metallurgical phenomena involved have left the vast majority of existing metals and alloys far from attaining the desirable attributes, and are even largely regarded as remaining in a non-usable state.[3] These Achilles' heels are related to the inherent characteristics of locally occurring rapid melting and solidification that impart uncontrolled microstructures and unpredictable mechanical properties to the manufactured products.[4] Hence, considerable efforts have been devoted to redesigning and expanding the material systems applicable to additive manufacturing for application requirements.[5–9] In general, conventional alloy design based on pre-alloyed feedstock (powders or wires) alone becomes unsuitable, because of the limited ability to further optimize alloy chemistries and costly expenditures.[10] Promoting additional alloying by bringing solute elements and secondary phases into the metallic alloy matrix has been proven to have significant potential,[11] such as a nanoscale oxide-dispersion-strengthened (ODS) NiCoCr alloy,[12,13] a bifunctional molybdenum additive stabilized metastable β titanium alloy,[14] and an intermetallic compound refined nonprintable aluminum alloy.[15,16] Notably, the direct incorporation of brittle secondary phases often results in an undesirable loss in the load-transfer strengthening effect owing to poor wettability and interfacial thermophysical property gaps.[17] Alternatively, although post-printing heat treatments can facilitate the precipitation of new phases through solid-state phase transformations and mitigate the chemical inhomogeneity in alloys, it might coarsen the grain structures, adversely affecting the mechanical properties.[18] Consequently, it is highly desirable to comprehensively consider the physicochemical properties of the target alloys to reconcile potential interactions and minimize the need for downstream heat treatments.

A further thorny dilemma is that many functional metallic alloys, which are compositionally sensitive, are inevitably exposed to a high energy input ($\sim 10^{5-7}$ W cm^{-2}) and large temperature gradients ($\sim 10^{5-6}$ K m^{-1}) during the additive manufacturing process.[19,20] It also results in their intended functional performances being particularly susceptible to impact, which poses an additional challenge for the specific applications of smart components made from these alloys. A typical example is the deterioration of the phase transformation behavior of nickel-titanium shape memory alloys (NiTi SMAs) due to the loss of the Ni element by evaporation.[21] The reason why these SMAs exhibit remarkable functional characteristics, such as the superelasticity effect (SE) and the shape memory effect (SME), is closely linked to stress-induced thermoelastic martensitic phase transformation (SIMT) and inverse martensitic phase transformation (IMT) occurring in the microstructures.[22,23] The alloy design for the secondary phase in such cases encounters non-negligible complexity and applicability difficulties and is thus forced to make trade-offs from numerous mutually exclusive relationships.[9] The confluence of these issues has made it exceedingly challenging to achieve balanced mechanical properties and functional performances directly in the as-printed state.

We present an *in situ* nanoscale heterostructure engineering (INSHE) strategy to address this challenge by precisely introducing a uniform dual nanoprecipitation through the *in situ* formation of nanoscale new phases and systematic engineering of heterostructures within functional metallic alloys. The INSHE design framework focuses on the controlled synthesis and lattice-matched assembly of nanocrystals to ''bottom-up'' modulate non-equilibrium microstructures. This advancement enables us to fully harness the exceptional properties of functional metallic alloy systems, such as NiTi SMAs,[19] in response to the increasing demand for structural complexity and functional integration. By overcoming the mechanical *versus* functional behavior trade-off through nanoscale synergistic deformation mechanisms—including locally shear-induced amorphization of the B2 matrix and crystalline fragmentation of dual nanoprecipitates—we have achieved an exceptional combination of mechanical properties and multifunctional responses directly from additive manufacturing. Furthermore, our approach offers significant advantages in printability for complex spatial structures, providing a framework that could inform the design of other alloy systems.

Results and discussion

Recent progress in AM has demonstrated the effectiveness of incorporating nanoparticles into metallic matrices, such as the GRX-810 system in which Y_2O_3 nanoparticles are introduced *via* powder coating and subsequently dispersed during AM.[12,13] While such oxide-dispersion strategies have achieved industrially relevant scalability and improved high-temperature performance, the conceptual foundation of INSHE is distinct. First, INSHE is a thermochemically guided, reaction-controlled strategy. By combining nanoparticle reactants (*e.g.*, B_4C) with thermodynamic modeling (chemical potential analysis and Gibbs free-energy predictions), we design laser-activated reactions that proceed within microsecond time scales inside the melt pool, producing new carbide/boride phases *in situ* rather than dispersing inert preformed particles (*e.g.*, TiO_2,[24] TiC,[25] and TiB_2[26]). Second, INSHE yields lattice-matched dual nanoprecipitates (TiC/TiB_2) with fully coherent interfaces, which assemble uniformly throughout the metallic matrix and provide unique interfacial strengthening and synergistic deformation mechanisms. In contrast, *ex situ* oxide-dispersion or non-reactive nanoparticle addition methods introduce stable oxide dispersoids that are well dispersed but lack such lattice-matched, chemically bonded dual-phase heterostructures (*e.g.*, Y_2O_3,[12,13] Al_2O_3,[27] and ZrO_2[28]). Third, while such *in situ* alloying,[5] *in situ* precipitation,[15] and oxide-dispersion[11,12] approaches have proven scalability in standard AM platforms, INSHE offers a more generalizable design framework: through reactant selection, reaction pathway control, and process optimization, it can be extended beyond B_4C/NiTi systems to a

broader set of ceramic-metallic matrix combinations, such as TiN/Al (yielding Al_3Ti/AlN) and BN/Ti (yielding TiB_2/TiN). Together, these distinctions highlight that INSHE represents not only a materials processing innovation but also a transformative design paradigm: it leverages in-melt chemistry and lattice-matched hetero-assembly to generate dual-nanoprecipitation and multi-functional performance that are fundamentally distinct from conventional *in situ* alloying, *in situ* precipitation, and *ex situ* oxide-dispersion or non-reactive nanoparticle addition methods.

Specifically, we have harnessed the extreme metallurgical environment of laser powder bed fusion additive manufacturing (LPBF-AM) and an adaptive alloy design strategy to enable dual-nanoprecipitates *in situ* embedded within eutectic colonies in near-equiatomic $Ni_{50.8}Ti_{49.2}$ (at%) SMAs. Through crystallographic design, we engineered the flawless nanoscale assembly of two distinct lattice structures—hexagonal structure (Hex) and face-centered cubic (FCC)—to create a unique reinforcement with ultrafine heterostructures. This differs from previous concepts in alloy design based on '*ex situ*' doping modifications, as the laser-excited transient nanometallurgical behavior during the build-up process will drastically modulate the non-equilibrium microstructures across multiple scales.[10] Fig. 1A schematically illustrates the design principle for creating dual-nanoprecipitates by lattice assembly in the *in situ* nanometallurgical SMA (INSMA hereafter). Specifically, boron carbide (B_4C) nanoreactants are used as *in situ* reactants, hydrostatically adsorbing onto and mixing with SMA micropowder to serve as the reaction medium. A detailed description of the powder preparation process can be found in the Materials and methods section. Subsequently, a high-energy-density laser beam selectively melts the powder feedstock while continuously driving thermochemical reactions in the micron-sized melt pool.[29] In this process, the SMA melt continuously supplies a stable titanium source, facilitating the rapid nucleation of free-state carbon and boron atoms, which preferentially grow with a low mismatch and a highly ordered interfacial structure. The subsequent rapid solidification ultimately results in the *in situ* formation of dual-nanoprecipitates within the matrix grain interior, consisting heterogeneously of titanium carbide (TiC, NaCl-type, space group $pm\bar{3}m$) and titanium diboride (TiB_2, C32-type, space group $P6/mmm$).

To elaborate the feasibility of tailored reaction paths from a thermodynamic perspective, we calculated both the phase diagram and the chemical potential diagram of the Ti–B–C ternary system to predict the relationship between constituent phases, the chemical potential of each element, and the stability region of each phase (Fig. 1B and C). Across a wide compositional space, TiC and TiB_2 emerge as the most energetically and structurally stable phases, favoring their *in situ* formation within the high-temperature melt pool—a prerequisite for controlled nanoprecipitate synthesis. To support this, we evaluated the temperature-dependent standard Gibbs free energy and enthalpy changes for all relevant reactions (Fig. S1 and Table S1). The target reactions exhibit a large negative standard Gibbs free energy change ($\Delta_f G^0_{298}$) and a standard enthalpy change ($\Delta_f H^0_{298}$) across the processing window (Table S2), indicating thermodynamic favorability and the potential for self-sustained exothermic reactions during LPBF-AM.[30] This suggests that ultrafast laser interactions with nanoreactant-functionalized SMA powders can reliably form lattice-matched TiC and TiB_2 nanoprecipitates within $\sim$80 μs. Additional validation is provided through convex hull and chemical potential analyses of relevant binary systems (Fig. S2), which reinforce the stability of the proposed phase configurations in the molten SMA matrix. This thermodynamically guided framework enables precise dual-nanoprecipitate formation through lattice-matched *in situ* reactions between tailored nanoreactants and the SMA matrix. The comprehensive thermodynamic analyses—including phase diagrams, chemical potential mapping, and Gibbs free energy calculations—collectively establish the viability of the INSHE strategy during LPBF-AM. While the martensitic phase transformation behavior is indeed a key factor governing the mechanical and functional properties of NiTi alloys, our experimental investigations systematically integrate both phase transformation characteristics and mechanical performance metrics, thereby providing a holistic validation of this approach. Importantly, the INSHE strategy is not confined to NiTi shape memory alloys. The thermodynamic design framework and *in situ* precipitation engineering demonstrated here are broadly applicable across a wide range of metallic systems. In particular, the methodology can be readily extended to Ti-based alloys and beyond through rational reactant selection and reaction pathway design. As a preliminary demonstration of its broader applicability, the INSHE strategy was also implemented in an additional Ti–6Al–4V alloy system (Fig. S47), where uniform nanoreactant-functionalized powders led to refined microstructures and the *in situ* formation of coherent dual-nanoprecipitates, thereby validating the versatility of the approach beyond NiTi alloys. To this end, we are currently employing high-throughput computational screening to identify compatible precursor–matrix pairs, with the aim of generalizing the INSHE strategy for the development of next-generation multifunctional alloys tailored for additive manufacturing applications.

The bright-field transmission electron microscopy (TEM) image (Fig. 1D) reveals the typical heterogeneous architectures in a dual-nanoprecipitate. More information on the morphology of the dual-nanoprecipitates diffusely dispersed within the B2 austenite matrix grains can be found in Fig. S3, with an average size of $\sim$100 nm. Among the observed precipitates, each of the ultrafine heterostructures had notable facets, indicating the presence of a preferred crystallographic orientation relationship (OR) between the two constituent phases.[31] We further conducted structural investigation on the interfacial features at the atomic and nanoscale. The high-resolution TEM (HRTEM) image (Fig. 1E) shows that the ultrafine heterostructure consists of nano-TiC as the primary nucleation phase assembled with nano-TiB_2 as the heterogeneous phase, as confirmed by the fast Fourier transform (FFT) pattern. According to high-angle annular dark-field (HAADF) scanning TEM (STEM) imaging and energy-dispersive x-ray spectroscopy (EDS) mapping (Fig. 1H), multiple intragranular concentration gradients are evident alongside the TiC–TiB_2-B2 interphase interface region, leaving a short-range diffusion zone of C

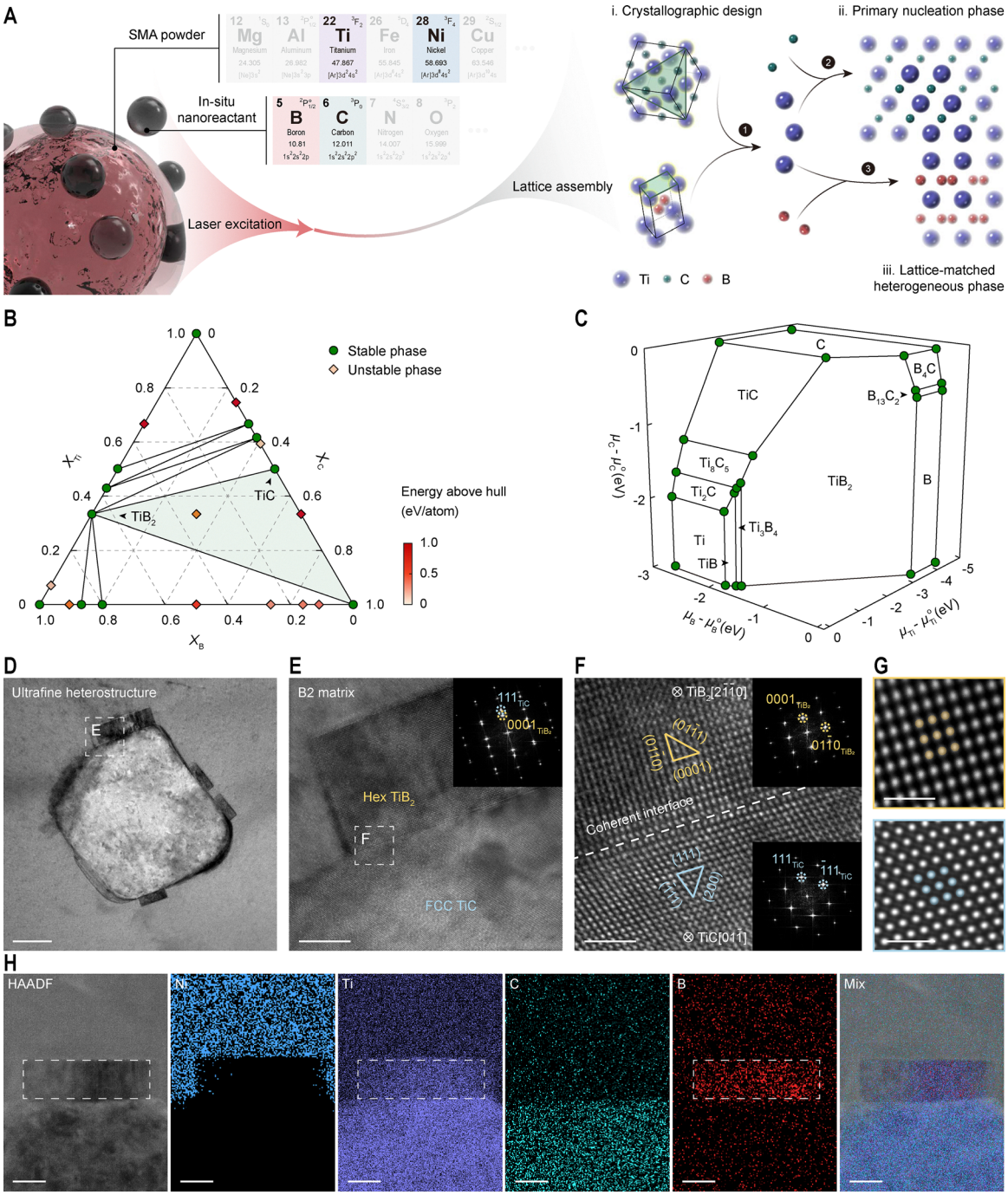

Fig. 1 Design, synthesis, and characterization of the INSMA. (A) Schematic illustration of the laser-excited lattice assembly process. Key reactants and low-energy-barrier epitaxial growth schemes are depicted, with lattice-matched planes in the unit cells indicated in green. Ternary phase diagram (B) and three-dimensional (3D) chemical potential diagram (C) for the Ti–B–C system (values are at%). (D) Bright-field TEM image of an individual dual-nanoprecipitate with ultrafine heterostructures. (E) High-resolution TEM (HRTEM) image and associated FFT pattern (inset) of the boxed region in (D). B2, ordered body-centered cubic; Hex, hexagonal; FCC, face-centered cubic. (F) HRTEM image of the boxed region in (E), showing the heterogeneous interface structure with full lattice coherence parallel to the close-packed $(111)_{TiC}$ and $(0001)_{TiB_2}$ planes. The insets are the FFT patterns of the corresponding phase structures. (G) Atomic-resolution TEM images showing the periodic atomic columns of the TiC nanophase (lower) and TiB_2 nanophase (upper) taken with the $[01\bar{1}]_{TiC}//[2\bar{1}\bar{1}0]_{TiB_2}$ zone axis. The stacking sequences of Ti atoms are marked in yellow and blue, respectively. (H) HAADF-STEM image and TEM-EDS elemental maps of the ultrafine heterostructure. Scale bars, 50 nm (D), 10 nm (E), 2 nm (F), 1 nm (G), and 20 nm (H).

and B elements at the outer edge. The observation taken along the $[01\bar{1}]_{TiC}//[2\bar{1}\bar{1}0]_{TiB_2}$ zone axis shows the presence of crystalline domains, and the acquired higher-magnification HRTEM images and associated FFT patterns depict the detailed nanostructures near the phase interface in the heterostructure (Fig. 1F and G). It is clear that the interfacial structure between

the TiC and TiB_2 phases displays full lattice coherence and has a preferential OR along the close-packed planes: $(111)_{TiC}$// $(0001)_{TiB_2}$ and $[01\bar{1}]_{TiC}$//$[2\bar{1}\bar{1}0]_{TiB_2}$, which verifies our original intention of designing the lattice-matching strategy. Moreover, the calibration results of the remaining partitioned heterostructures in Fig. 1D after specific indexation are shown in Fig. S4. We found that all ultrafine heterostructures at different partitions have an equivalent OR and a typical coherent interface without mismatch dislocations. Even the structural analysis of other dual-nanoprecipitates undergoing lattice assembly matches perfectly with the above features (Fig. S5).

In essence, laser-excited thermochemical reactions aim to minimize the critical nucleation energy barrier for the system in the vast majority of the cases.[32] The primary precipitation of the TiC phase in the B2 matrix provides perfectly flat and clean bare interfacial sites for the heterogeneous nucleation and growth of a lattice-matched TiB_2 phase. On the other hand, as the B_4C nanoprecursors were involved in the *in situ* reaction in the molten pool, they would be spontaneously and continuously consumed and eventually used up. The exsolution of C atoms with the TiC phase causes the B atoms to be expelled to the solid–liquid (S–L) interface, *i.e.*, the solidification front,[33] creating an elemental aggregation zone, which, in turn, promotes the formation of the B-rich TiB_2 phase. Consequently, a symbiotic relationship between the TiC phase and the adjacent TiB_2 phase can be identified. Notably, when the spatial dimensions of the primary nucleation phase are too small (less than 50 nm), it is frequently unable to *in situ* generate a heterogeneous phase (Fig. S6). The symbiotic mechanism demonstrates that this is attributed to the presence of a large boundary curvature at the primary stage, and the B-atom concentration aggregated by solute redistribution has not yet reached the critical nucleation threshold. In Ti-rich alloy melts, the driving force for the growth of TiC crystal nuclei is the continuous diffusion of supersaturated free-state C atoms in the liquid phase to the phase interface.[34] Nevertheless, once the TiB_2 lattice groups begin to be assembled and deposited on its surface, short-range diffusion along the close-packed planes to which they are docked will be impeded. The TiC lattice then turns to expand to both sides, thereby developing significant bulges, while the TiB_2 lattice can only be stacked along the longitudinal direction at this time (Fig. S3G–I). Benefiting from the combined constraints of minimized lattice misfit, similar atomic packing along matched crystallographic planes, and thermodynamic stability in the desired products, this unique configuration strategy, which is both synergistic and competitive, facilitated the precise *in situ* synthesis of fine dual-nanoprecipitates. Although the current mechanistic understanding primarily relies on *ex situ* HRTEM/STEM observations combined with thermodynamic calculations, future integration of time-resolved *in situ* characterization techniques, such as *in situ* high-energy X-ray imaging,[35] *operando* synchrotron X-ray diffraction,[36] and *in situ* neutron diffraction,[37] may offer direct insights into the nucleation barriers and growth kinetics of dual-nanoprecipitates during rapid solidification (cooling rates $\sim 10^{3-6}$ K s^{-1}) in AM, particularly their dependence on processing parameters (*e.g.*, laser power and scan speed).

To gain a deeper insight into the non-equilibrium solidified microstructures, we performed electron backscatter diffraction (EBSD) characterization of as-printed SMAs. Reconstructed 3D views of the EBSD inverse pole figure (IPF) maps depict the spatially dependent grain structure features, including the grain morphology and crystal orientations (Fig. 2A). The microstructures of pristine SMAs mainly consist of elongated columnar grains across multiple molten pools along the build direction (BD). The presence of severe ⟨001⟩ and ⟨101⟩ orientations due to epitaxial growth in these coarse grains, exhibiting a strong typical ⟨100⟩//BD fiber texture (Fig. S7A), is also evidenced by XRD analysis (Fig. S19A). Although the rapid solidification rates associated with the LPBF-AM process are conducive to achieving refined microstructures, the easy growth directions of grains tend to correlate closely with the maximum temperature gradient of the melt pool owing to the need to balance the heat flux distribution.[15] This phenomenon was commonly observed in BCC metals with poor thermal conductivity, particularly when subjected to temperature distribution restrictions characterized by repetitive thermal cycling.[38] The resulting preferential solidification drives continued grain growth vertically through the partially melted layers and eventual dominance, which will inevitably exacerbate mechanical property anisotropy. Comparatively, it can be noticed that the grain structure and the relevant crystalline texture of our INSMA undergo a slight modulation and the orientation distribution is more random, although the epitaxial growth trend persists (Fig. 2A and Fig. S7B). Close examination of the microstructure reveals that the columnar growth of a small fraction of the B2 austenite grains was interrupted [side view along the transverse direction (TD)]. The reason is that the disturbing effect of the thermochemical reactions occurring in the molten pool on the Marangoni flow makes the grain growth orientation unaligned with the heat flow direction. Thus, the average grain sizes and aspect ratios of the INSMA are shifted towards lower values compared with the pristine SMA (Fig. S8).

We further present the resultant maps based on on-axial, high-precision transmission Kikuchi diffraction (TKD) observations to illustrate the dual-nanoprecipitation configuration at both the micro- and nanoscale (Fig. 2B, C and Fig. S7C, D). Phase maps show the dual-nanoprecipitates diffusely distributed in the B2 matrix, consistent with the TEM results (Fig. S3). Correspondingly, the image quality (IQ) plus grain boundary (GB) maps reveal the low-angle GBs ($2^\circ \leq$ LAGBs $\leq 15^\circ$) between the dual-nanoprecipitates and the B2 matrix. The nearly zero lattice misfit is located in heterostructure regions because of the strong coherency, and their misorientation angles are below the minimum evaluated value ($<2^\circ$). In addition, the kernel average misorientation (KAM) maps provide the localized misorientation distribution within the matrix grains. A brighter color indicates a greater orientation deviation from the reference value, which is defined as the average orientation of the grain. It is evident that high KAM values are predominantly concentrated surrounding the dual-nanoprecipitates, which are considered as rearrangement and intensive accumulation of interface dislocations.[39] This observation indicates a positive correlation between KAM distribution and the fraction of LAGBs in non-equilibrium

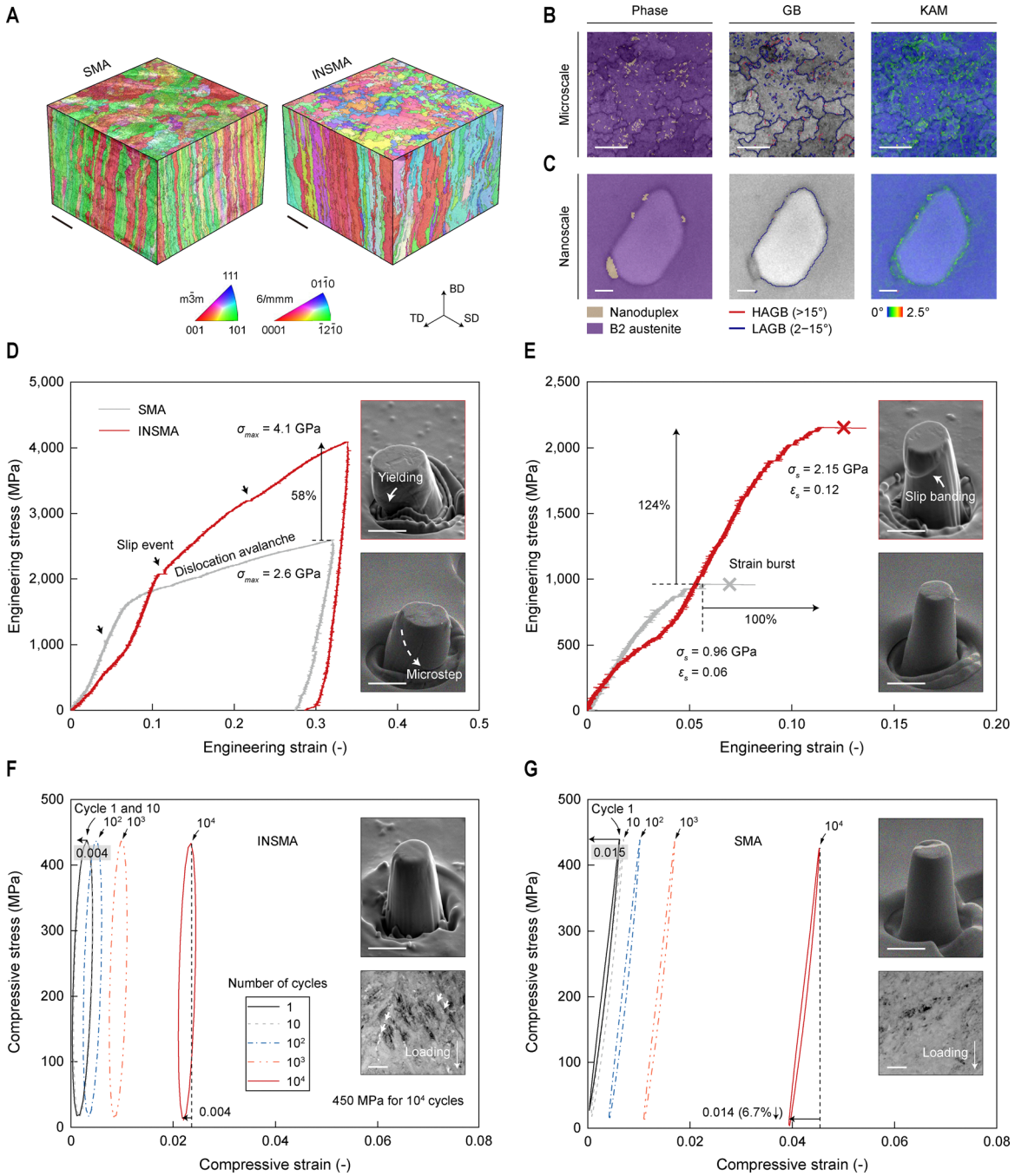

Fig. 2 Microstructures and mechanical properties of SMAs. (A) Reconstructed 3D views of the crystallographic orientation from EBSD IPF maps along the scan direction (SD), the transverse direction (TD) and the build direction (BD). (B) and (C) TKD resultant maps of the INSMA sample viewed along the BD, showing the distributions of phase, two types of boundaries defined with different misorientation angles, and local misorientation. Note that the TiC nanophase cannot be indexed in the phase map due to its close crystal structure to the B2 matrix. LAGB, low-angle grain boundary; HAGB, high-angle grain boundary; KAM, kernel average misorientation. (D) The plastic stress–strain responses and morphologies (the insets showing SEM images viewed at 55° tilting) of SMA (lower) and INSMA (upper) micropillars after monotonic compression. (E) The critical engineering stress–strain curves related to initial strain burst phenomena. (F) and (G) The cyclic stress–strain responses, morphologies (the top right insets show SEM images) and deformed nanostructures (the bottom right insets show TEM images) of INSMA (F) and SMA (G) micropillars subjected to 10^4 cycles of compression under stress of 450 MPa. The thick white arrows in the bottom right TEM image show the location of dual-nanoprecipitates. Scale bars, 100 μm (A), 5 μm (B), 50 nm (C), 2 μm (D), (E), and the top right insets of (F) and (G), and 200 nm (the bottom right insets of (F) and (G)).

microstructures, along with evidence of reaching higher average levels in the INSMA relative to the pristine SMA (Fig. S9 and S10). This large number of LAGBs arising from dual-nanoprecipitation behaviors are directly responsible for dislocation multiplication in the parent phase. We attribute the emergence of interfacial dislocations in our INSMA to lattice misfit at the nanoprecipitate–B2

interface, which further develops into the dislocation walls (*i.e.*, subgrain boundaries) constituted by large-scale mismatched dislocation networks in localized regions. The accumulation of stored distortion energy associated with these remarkable microstructural evolutions is advantageous for enhancing the mechanical properties and is expected to produce intense hetero-deformation-induced (HDI) strengthening and strain hardening.

Two different SMAs from our work were tested by quasi-static micropillar compression at a rated strain of 30% to compare their plastic stress–strain responses (Fig. 2D). *In situ* recorded load-displacement data were converted into nominal stress–strain curves to eliminate size-dependent errors. The INSMA we examined has an ultrahigh compressive strength (σ_{max}) of 4.1 GPa and exhibited an extraordinary strain hardening capability during the plastic deformation stage. The substantial increase in deformation resistance (up to 2 GPa) primarily arises from Orowan mechanism-related dislocation avalanches during extrusion upsetting, which markedly surpass that of the pristine SMA. The uniaxial tensile and compressive test results of the printed macroscopic specimens of both the pristine SMA and INSMA at room temperature also show the advantage of the INSHE strategy (Fig. S40). One notable observation is the occurrence of non-uniform deformation characterized by a low slope strain plateau in the INSMA, accompanied by delayed yielding (Fig. 2D, top right inset, and Movie S1). We also found multiple crossover slip bands and bulges emerged at the surface of the micropillar after plastic yielding (Fig. S11A–C). In the absence of any pinning effect, the pristine SMA micropillar continuously slides and ultimately overflows the surface under elevated shear to develop a submicron-scale step (~185 nm) (Fig. 2D, bottom right inset, and Movie S2). To elucidate the underlying synergistic deformation mechanism originating from the in-grain dual-nanoprecipitates, we examined the postmortem nanostructures of INSMA micropillars. Under large plastic deformation, we detected the shear-induced amorphization exemplarily found in previously studied nanocrystalline NiTi micropillars.[40] The HRTEM observations suggest that the amorphous phase was formed in the region with strong plastic strain localization, whereas the polycrystalline phases with interface dislocations were formed in the less-strained region (Fig. S11D–G). Correspondingly, the masked FFT pattern revealed the coexistence of B2 austenite and B19′ martensite in the polycrystalline phases (Fig. S11G, inset). Except for amorphization, plenty of nanocrystallites generated by the dual-nanoprecipitate interacting with dislocation activities appear in the B2 matrix (Fig. S11H and I). They initially evolved from intensive lattice shearing within the dual-nanoprecipitates at dislocation avalanches.[41] The formation of numerous nanocrystallites through crystalline fragmentation of dual-nanoprecipitates is a critical finding in the INSMA under extreme loading, as this mechanism not only allows them to accommodate severe deformation but also introduces ductility through sequential torsion with ongoing deformation.

To investigate the initial strain burst ('pop-in') phenomenon, we provide the critical stress (σ_s) and strain (ε_s) values related to slip banding, as shown in the engineering stress–strain curves in Fig. 2E. The results revealed that, unlike in the pristine SMA, the critical stress and strain required to induce the start of the strain burst in the INSMA were considerably increased, by approximately 124% and 100%, respectively. This observation was similar to the mechanical behavior of micropillars before yielding when subjected to a plastic strain of ~30%, which collectively suggests an enhanced shear resistance by diffusely distributed dual-nanoprecipitates impeding dislocation movements (Movies S3 and S4). At a medium compressive strain of ~12% reaching the strain burst point, we observed stacking slip bands close to 45° at the surface of the INSMA micropillar (Fig. 2E, top right inset, and Fig. S12A–C). The features of the associated slip-deformed matrix were uncovered using the inverse FFT (IFFT) image recorded along the reciprocal lattice vectors $g(1\bar{1}0)$ (Fig. S12G), which showed distorted lattice fringes and widespread dislocations in the B2 matrix. The shear-induced amorphization was not obvious (Fig. S12D–F) and the dual-nanoprecipitates therein maintained an intact crystalline structure (Fig. S12H and I), attributed to the dislocations having to overcome the high strength level of lattice distortions for further slip and penetration. These slip events are triggered by intermittent strain bursts, which are intrinsically contingent upon the unstable kinetic behaviors of the microscopic deformation activated after the stress-induced phase transformation from B2 austenite to B19′ martensite.[42] Furthermore, the fatigue performances of the micropillars were evaluated by subjecting them to 10^4 cycles of compression under stress of 450 MPa (Fig. 2F and G). The pristine SMA showed prominent functional degradation, where the recoverable strain (ε_{rec}) decreased by 6.7% and the residual strain (ε_r) reached 4%, after 10^4 cycles of compression. The reduction in cyclic stability reflects the presence of reversible phase transformation induced dislocations that result from microscopic strain incompatibility at the moving phase boundaries (habit planes).[43] Considering the relatively higher B19′ phase fraction in the pristine SMA's phase composition (Fig. S19), the reorientation of B19′ martensite variants during cyclic loading can serve as a contributing factor in the accumulation of residual strains. In contrast, under the same cyclic stress and cyclic period, we confirmed in the INSMA a larger hysteresis loop area (A) and a roughly halved residual strain, with negligible losses in deformation recovery and energy dissipation capabilities. At a low strain of ~2% caused by fatigue, we detected the R phase, a typical transformation intermediate common in NiTi SMAs (Fig. S13D). The R phase's low strain characteristics, high reversibility, and stress-dispersing capability can significantly enhance the low-cycle fatigue life and cyclic stability, whereas the accumulation of concentrated dislocations at the R-phase/parent-phase interface and the superposition of multiphase transformations may exacerbate fatigue damage at the high-cycle stage. The surface of the INSMA micropillar remained very smooth throughout cyclic loading with no major difference from the just-fabricated state, and the postmortem nanostructure showed a few concentrated dislocations with a Burgers vector of $a\langle 001\rangle$ contained within the monocrystalline B2 phase, as we confirmed by HRTEM images at the deformation stage of ~12% strain (Fig. S13 and Movie S5). In particular, this suggests that the material is endowed with a more stable cyclic

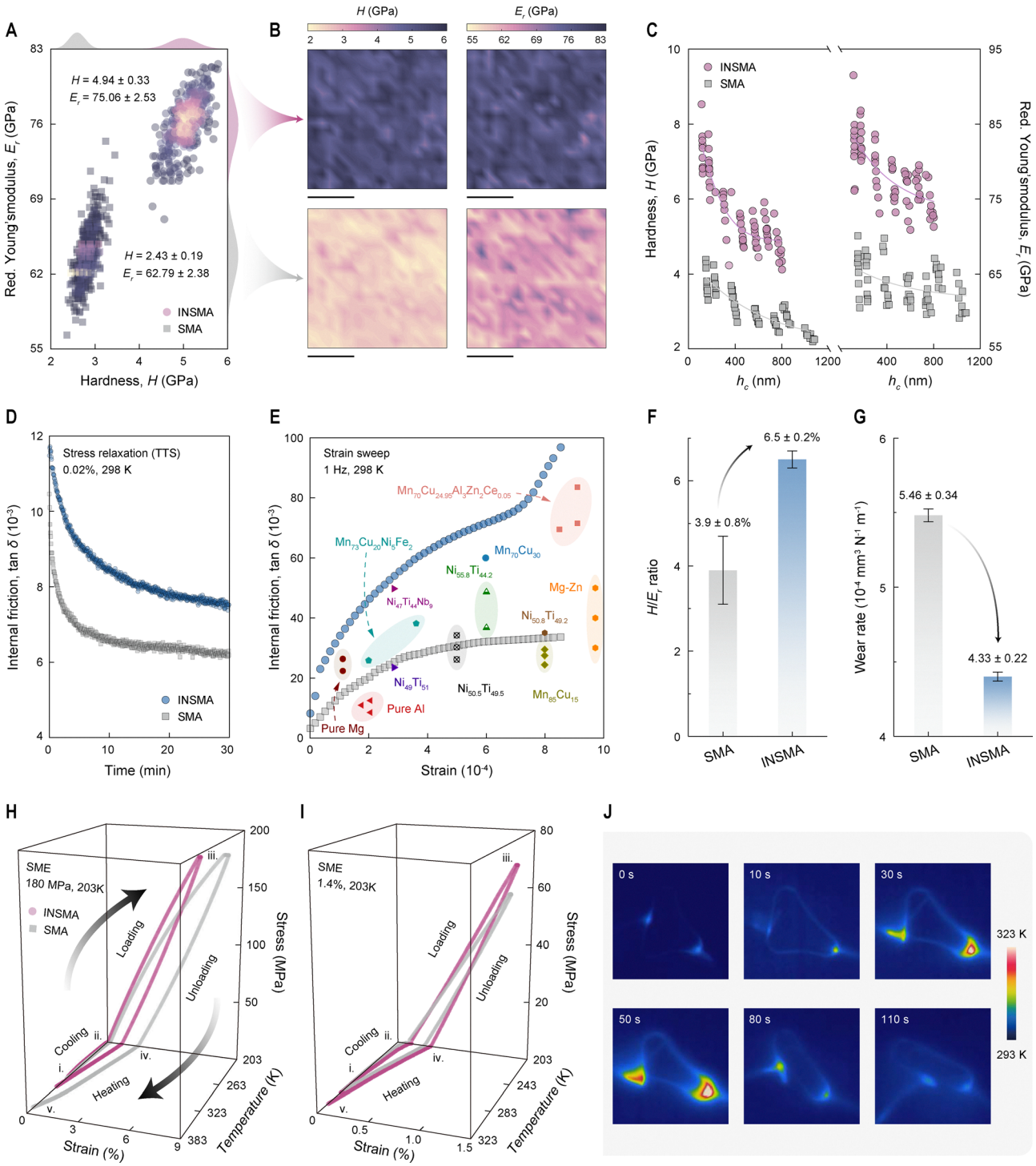

Fig. 3 Multifunctional responses of SMAs. (A) The discrete 2D histogram of hardness (H) *versus* reduced Young's modulus (E_r), showing data from 400 nanoindentation measurements. (B) The corresponding hardness and reduced Young's modulus distributions from high-speed nanoindentation mapping. (C) Plots of hardness and reduced Young's modulus as a function of contact depth (h_c), showing data from 70 nanoindentation measurements. Plots of damping capacity (internal friction, tan δ) as a function of relaxation time (D) and strain amplitude (E) for stress relaxation and strain sweep conditions, respectively. A comparison of the current alloys against other reported metallic materials with high damping capacity, including pure Al, pure Mg, Mg–Zn alloys, Ni–Ti- and Mn–Cu-based SMAs, is summarized in (E). TTS, Time-temperature superposition. (F) and (G) H/E_r ratios (F) and wear rates (G) of SMAs. The error bars represent standard deviations. (H) and (I) Plots of thermomechanical stress–strain–temperature curves showing the shape memory effect (SME) responses from multistep dynamic mechanical analysis (DMA) experiments with specific stress (H) and strain (I) applied, respectively. (J) Infrared images showing the visually actuated demonstration of the shape recovery behavior for an INSMA 'paperclip'. Scale bar, 100 μm (B).

response, thereby making the actual fatigue life well exceed the achieved 10^4 cycles. Although *in situ* TEM under mechanical loading was not accessible, our postmortem TEM analyses at different deformation levels (Fig. S11–S13), combined with geometric phase analysis (GPA) based strain mapping (Fig. S5), provide indirect evidence that the coherent interfaces between dual-nanoprecipitates and the B2 NiTi matrix promote nanoscale deformation mechanisms that resist shear-induced amorphization and support the enhanced mechanical and functional performance of the INSMA.

Subsequently, we conducted high-speed nanoindentation mapping to assess the distribution and stability of the nanomechanical properties of SMAs (Fig. 3A–C). This high-throughput characterization approach allows for parsing the local variations in mechanical responses induced by dual-nanoprecipitation, while facilitating distribution statistics. Our INSMA exhibited significantly higher average hardness (H) and reduced Young's modulus (E_r) values at a maximum applied load of 50 mN [as determined by continuous stiffness measurements (CSM), Fig. S14], compared to a more than two-fold increase in hardness even over the pristine SMA (4.94 $\pm$ 0.33 GPa *versus* 2.43 $\pm$ 0.19 GPa) (Fig. 3A and B). Moreover, we found that the hardness and reduced Young's modulus decreased with increasing indentation depth in the contact depth (h_c) range of 100–1100 nm (Fig. 3C and Fig. S15). Such an indentation size effect revealed the dependence of the nanomechanical properties on the trial depth and can therefore be well described for their stability. Despite the distributions of the nanomechanical properties all tending to be homogeneous, the values measured in the INSMA were markedly more scattered (Fig. 3A). The differences in the indentation morphology at high magnification explained this observation (Fig. S16), attributed to the small size of dual-nanoprecipitates, which resulted in matrix mixing within the indentation volume. The ratio of hardness-to-reduced Young's modulus (H/E_r) is an important characteristic value for analyzing the friction and wear behavior of superelastic materials.[44] The H/E_r ratio of the INSMA we examined reached 6.5 $\pm$ 0.2% compared to the pristine SMA (only 3.9 $\pm$ 0.8%), which is consistent with further tribological results (Fig. 3F, G and Fig. S17). The worn surface morphology indicated that INSMA's excellent wear resistance was derived from the formation of lubricating oxide films on its high hardness surfaces, which were typically characterized by an adhesive wear mechanism (Fig. S18). The synergistically enhanced resistance to plastic deformation plays a crucial role in inhibiting brittle microcrack extension, groove deepening and wear debris spalling. The dual-nanoprecipitates we introduced acted as reinforcements, substantially strengthening the SMA matrix, with reported values surpassing those of previous studies.[45,46] In addition, the wearing properties of NiTi alloys are also largely affected by the unique transformation behavior. The wear resistance advantage of the INSMA arises from its super-elasticity emphasized by SIMT, which enables dynamic hardening and partially recoverable deformation, ultimately contributing to reduced wear rates. In contrast, the pristine SMA primarily resists wear through stress-induced reorientation of martensitic variants and twin boundary sliding, with the coordination between the SME and plastic deformation contributing relatively little to wear resistance. Electrochemical measurements consistently show that the surface-modified INSMA exhibits lower corrosion current density, higher polarization resistance, and a more stable passive film than pristine SMA. These results confirm its markedly enhanced corrosion resistance across open circuit potential (OCP), potentiodynamic polarization, and electrochemical impedance spectroscopy (EIS) analyses (see SI 12).

Utilizing the time-temperature superposition (TTS) principle,[47] we explored the damping capacity (internal friction, $\tan\delta$) of SMAs by stress relaxation at a low strain level of 0.02% (Fig. 3D). Due to the recovery stage of elastic deformation similar to the 'clockwork' release, the stored residual stresses decreased rapidly within the early $\sim$10 min dwell time and then leveled off. After the final relaxation at room temperature for 30 min, we detected the loss factor of the pristine SMA plummeted to 6.2×10^{-3}. In contrast, the INSMA still maintained a rather high stress relaxation resistance (up to 7.6×10^{-3}). The activation energy required for dislocation motion gradually decreases during residual stress release. The dislocation network pinned by the dual-nanoprecipitates in the microstructural configuration participates in energy dissipation *via* dislocation unpinning, gliding, and repinning, thereby contributing to the damping capacity. Meanwhile, the twin boundaries between variants and the austenite/martensite (A/M) phase boundaries induced by the earlier martensitic transformation undergo localized reorientation. The dual-nanoprecipitates located at these interfaces readily increase the frictional resistance to twin boundary migration and grain boundary sliding, which further improves internal friction. We further present the damping capacity variations recorded by strain sweeps at a frequency of 1 Hz over a strain amplitude range of 0–9×10^{-4} to illustrate the energy-absorbing characteristics during mechanical vibration, as shown by the curves consisting of correlated data points in Fig. 3E. Undoubtedly, the damping capacity of the INSMA shows a significantly increasing trend, especially at relatively large strain amplitudes (over 8×10^{-4}), which is then nearly 2–3 times that of the pristine SMA. These distinct functional performances arise from a reversible martensitic transformation that occurs within its microstructural configuration. The increased mobility of internal boundaries facilitated the movement of boundaries under alternate stress to achieve sufficient dissipation of vibrational energy to the surrounding environment.[48] Analysis of the literature reveals that our LPBF-AM as-printed state INSMA gives superior reported values for damping response over a wide strain range than the multicomponent and commercial Snoek-type high-damping alloys produced by traditional time-consuming and energy-intensive thermomechanical processes, *e.g.*, melt-casting,[49,50] forging,[51] sintering,[52] pressure infiltration,[53,54] and post-treatment.[55,56] In addition, we performed thermomechanical shape memory experiments within a low-temperature window in the martensitic state to illustrate the material's stress–strain-temperature responsive nature (Fig. 3H and I). The phase transformation temperatures (TTs) and enthalpies were accurately determined from differential scanning calorimetry (DSC) thermograms (Fig. S19 and Table S3). The INSMA displayed typical linear

elastic behavior during high-stress forward loading at 203 K, whereas the pristine SMA prematurely converged to nonlinear deformation behavior (Fig. 3H). Indeed, no obvious nonlinearities similar to those mentioned above were developed when applying lower pre-strains (Fig. 3I). It should be emphasized that this difference in apparent loading-unloading behavior stems from the plastic deformation due to the low matrix strength in the pristine SMA. In the heating range from the martensitic transformation finish temperature (M_f) to the austenitic transformation finish temperature (A_f), the unloaded residual strain undergoes a large-scale strain recovery by the reverse martensitic transformation (M to A) (Fig. S20). As a result, the INSMA was found to maintain a nearly ideal shape recovery rate (R_r) comparable to those of the majority of Ni-rich and near-equiatomic NiTi SMAs. As an important aspect of demonstrating the ability to memorize permanent shapes, a machined INSMA filament is mechanically deformed into a 'paperclip' in a high-temperature austenitic state (Fig. 3J). After removal of the deformation force allows fixing of this set shape, it is transferred back to room temperature which completes the programming step. After switching to any temporary shape, it was connected to a regulated DC circuit supplied by a source meter. It can be noticed that infrared temperature monitoring demonstrates that the heat transport resulting from the Joule heating effect actuated the paperclip to complete the programmed shape recovery within 110 s.

Given the synergistic strengthening potential offered by dual-nanoprecipitation, we have fabricated four types of shape-memory mechanical metamaterials (SMMMs) with representative topological microarchitectures by leveraging the flexibility of LPBF-AM. One prominent feature of these SMMMs is that their structural porosity decreases sequentially, while the relative density increases accordingly (Fig. S21). As shown in zoomed-in SEM images (Fig. 4A and Fig. S22), we examined an unprecedented printing fidelity in as-built SMMMs. The surface finish of the pristine SMA microlattices is suboptimal, with poorly fused powder particles adhering to both the nodes and struts, accompanied by several obvious nodules. This phenomenon must not be overlooked, as rough surfaces tend to become nucleation sites for cracks during deformation, leading to a substantial reduction in the material's damage-tolerant load-bearing capacity.[57] To a certain extent, our INSMA counterparts provide a distinct advantage in printability, with deposited traces displaying an acceptable surface morphology and stable processed dimensions. We further conducted a quantitative analysis to assess dimensional accuracy by 3D surface profile measurements, which revealed that several surface roughness indicators were simultaneously reduced for the INSMA relative to the pristine SMA (Fig. S23 and Fig. S24E–G). It was also found that the surface roughness of SMMMs was positively correlated with their structural porosity. For printing of dense bulk materials, the formation of squamous discrete bands on the printed surface results from layer-by-layer stacking of molten pools under a continuously moving high-energy laser beam (Fig. S24A–D). The well-fused surface states of our INSMA caused a corresponding decrease in the contact angle (Fig. S25). To rigorously disentangle the respective contributions of physical and chemical factors to this phenomenon, additional XPS characterization (Fig. S42) and contact angle measurements (Fig. S43) were performed on both pristine SMA and INSMA samples after surface polishing. The survey and high-resolution XPS spectra (Ni 2p, Ti 2p, C 1s, and B 1s) revealed no significant differences in the chemical composition, elemental valence states, or surface energy components, and the contact angles of the two materials were nearly identical under smooth and flat surface conditions ($\sim 52^\circ$). These findings indicate that the influence of chemical factors from surface modification by nanoparticles can be safely ruled out, thereby confirming that the reduced contact angle of the INSMA arises reliably from its substantially lower surface roughness compared to the pristine SMA, which directly accounts for the enhanced surface wettability and hydrophilicity (see SI 9). 3D visualization images reconstructed by microfocus computed tomography (micro-CT) further verified the feasibility of INSMA's overall optimization on internal quality (Fig. S26 and Movie S6). This observation contrasts strikingly with the manufacturing accuracy limitations in previous studies,[58] which were particularly prevalent when forming complex spatial structures. We attribute the disappearance of powder adhesion and rough surface in our INSMA lattices to the elevated energy absorption efficiency of the functionalized powder under laser radiation coupled with the extended thermal history encountered during the thermochemical reaction (Fig. S33 and Table S2). Under the extreme non-equilibrium solidification conditions of L-PBF, the additional thermal effects resulting from the reduced laser reflectivity of the powder (down 46%) and the exothermic heat released from internal reactions ($\Delta_f H^0_{298} = -743.078$ kJ mol^{-1}) altered the temperature gradient distribution within the tiny melt pool. This leads to higher liquid-phase temperatures and longer residence times, which allows the alloy melt a sufficient time for smooth wetting and spreading. We also found that this prominent heat generation can compensate part of the laser heat source to avoid the detrimental effects by overheating evaporation due to high laser power density, which causes Ni element loss and surface balling. Consequently, the above behavior facilitates the elimination of powder adhesion and rough surface features caused by inadequate melting during the printing of high-resolution, intricately detailed complex spatial structures.

The mechanical properties of all as-printed SMMMs were further evaluated under cyclic and gradient loads with a maximum applied strain of 10%. The INSMA-type mechanical metamaterials we examined exhibited excellent strain recovery behaviors after 10 cycles of compression training, while providing higher strength *versus* pristine SMA-type (Fig. 4B and Fig. S27). These advantages are also quite obvious in the gradient stress–strain responses acquired with the maximum strain level increasing from 2% to 10% (Fig. 4C and Fig. S28). To demonstrate and scale up the potential applications of the designed INSMA, we carried out quantitative analysis on its unique mechanical response. Of particular note, the obtained stress–strain curves provided valuable information regarding the characteristic strains and characteristic energies. We found that as the maximum strain level or the number of cycles intensified, both the amelioration in the elastic recovery strain (ε_{el}) value and the elimination in the

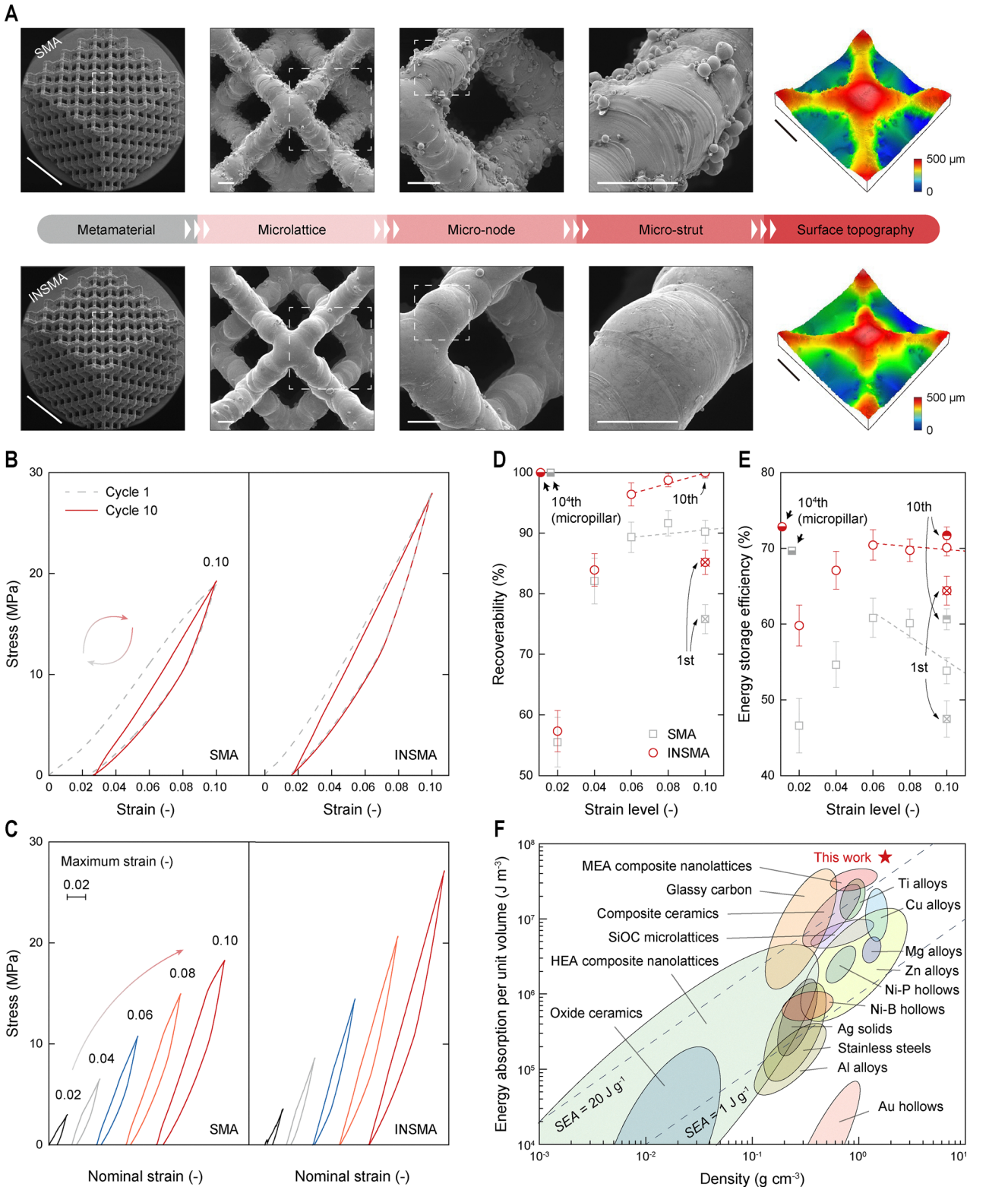

Fig. 4 Cyclic phase transformation-actuated adaptive SMMMs. (A) SEM images of as-printed SMMMs with zoomed-in views of the surface morphology. The 3D surface topographies on the right confirming the difference in print fidelity. (B) Cyclic stress–strain curves of dode-thin microlattice architected SMMMs subjected to 10 cycles of compression training at constant strain level of 10%. (C) Gradient stress–strain curves of SMMMs subjected to compression training at different maximum strain levels ranging from 2% to 10%. Summary plots showing the variation of recoverability (D) and energy storage efficiency (E) as a function of maximum applied strain. The thick black arrows showing the *in situ* micropillar compression data. (F) Ashby plot of energy absorption per unit volume *versus* density for the INSMA-type mechanical metamaterial, compared with other reported micro-/nanolattices and a wider range of functional materials (see also Table S7 for detailed testing parameters of the comparative lattices). M/HEA, medium-/high-entropy alloy; SEA, specific energy absorption. Scale bars, 5 mm (A, left), 200 μm (A, middle), and 500 μm (A, right).

irreversible strain (ε_{ir}) value of the INSMA greatly exceeded those of the pristine SMA, while the superelastic strain (ε_{se}) value differed little (Fig. S29). For instance, at a gradient strain level of 10%, the ε_{el} and ε_{ir} values were determined to be 3.4% and 0.7%, respectively, for the pristine SMA and increased to 4.8% and decreased to zero for the INSMA, respectively. Based on this trend, Fig. 4D depicts in detail the positive correlation between the strain level and recoverability [*i.e.*, the ratio of recoverable strain to total applied strain (ε_{tot})]. Linear fitting of the scattering points stabilized at high strains revealed that the INSMA exhibited a higher slope of the fitted line, culminating in a 100% recoverability. These commendable characteristics are contingent upon the activation of correspondent variant pairs (CVPs), representing two twin-related martensitic variants,[59] during cyclic phase transformation and grain reorientation. When the partially reoriented martensite induced to form by mechanical stress was stabilized by the multiplying activated dislocations, as reflected in the conventional SMAs, it resulted in retaining stabilized martensite that failed to be activated by free energy and elastic strain energy during the whole cyclic loading process.[60,61] In addition, the quantitative results on the integral area in Fig. S30 showed that our INSMA still maintained its finite dissipated energy ($E_{dissipated}$) with around twofold gain in absorbed energy ($E_{absorbed}$). This facilitates an overall improvement in their energy storage efficiency [*i.e.*, the ratio of absorbed energy to total energy (E_{tot})] and slows down the decreasing trend at high strains (Fig. 4E), which is well supported by the fatigue behavior observed under micropillar compression (Fig. 2F). Thus, unlocking the energy absorption characteristics of SMMMs actuated by cyclic phase transformation is indeed a notable achievement. We demonstrate an Ashby plot of energy absorption per unit volume *versus* density for the INSMA-type mechanical metamaterial in the present work and compared with other reported micro-/nanolattices[62–64] and a wider range of functional materials[65,66] (Fig. 4F and Fig. S41). To ensure transparency and improve the comparability of the Ashby plot, the detailed testing parameters (including the strain rate, number of cycles, and sample topology) of the comparative micro-/nanolattices are summarized in Table S7. To further ensure the reliability of the reported mechanical and functional properties, detailed statistical analyses were performed. The mean values and standard deviations of key parameters, including hardness, yield strength, compressive strength, energy absorption per unit volume, damping capacity, shape recovery rate, and other related metrics, are summarized in Fig. S46 and Table S10. These results confirm the reproducibility of the measured properties and provide a statistically robust basis for comparison. Generally, the energy absorption of our adaptive SMMM outperforms the majority of composites and technical ceramics with micro-/nanolattice architectures and surpasses these by 2–3 orders of magnitude when compared to some functional metallic materials with ductile structures (*e.g.*, hollow Au, Ni–B, and Ag). An in-depth analysis of the specific energy absorption (SEA) as a critical application parameter suggested that the adaptive SMMM reached an unprecedented specific energy absorption of 25 J g^{-1}, which broke through the well-known performance bottleneck of 1 J g^{-1} to 20 J g^{-1} for structural materials with low solid densities. Such resilience to energy absorption actuated by cyclic phase transformation is regarded as sustainable, together with the rarely observed multiple synergistic strengthening mechanisms unleashed by *in situ* dual-nanoprecipitation, thus promising to build upon by exploring the topological architectures for further well-designed and targeted adaptive materials.

Conclusions

In conclusion, we present an adaptive alloy design strategy, called INSHE, that involves *in situ* heterostructure engineering of nanoscale lattice assemblies within functional SMA systems to effectively address the complex trade-offs between printability, mechanical properties and functional performances in additive manufacturing. Our approach leverages laser-excited transient nanometallurgical processes to induce dual-nanoprecipitation, fostering a synergistic and competitive interplay between phases and modulating otherwise uncontrollable non-equilibrium microstructures. This adaptive alloy, featuring artificial nanocomposite microstructures, exhibits an exceptional combination of mechanical properties and multifunctional responses, including enhanced cyclic stability through reversible phase transformations and superior printability for complex spatial structures. Compared to the conventional wisdom in the SMA community, this demonstration shows markedly improved damping capacity, achieves linear elastic behavior throughout transformation temperatures, and maintains a close to ideal shape recovery rate, leading to greater actuation efficiency than existing multicomponent and commercial Snoek-type high-damping alloys. The INSHE strategy has the potential to be applied to other alloy systems, providing a pathway to advance additive manufacturing technologies and tailor materials for specific applications. Looking ahead, we acknowledge that extended thermal aging experiments at elevated temperatures will be essential to rigorously assess precipitate coarsening and long-term property retention, and we plan to address these aspects in our future work.

Author contributions

G. J. C. and J. Y. conceived this study. J. Y. carried out the experimental treatments, material characterization and data analysis. J. Y. and G. J. C. wrote the draught of the paper. G. J. C. supervised the project. All authors discussed the results and commented on the paper.

Conflicts of interest

The authors declare that they have no competing interest.

Data availability

All data needed to evaluate the conclusions in the paper are present in the paper and/or its supplementary information (SI). Supplementary information is available. See DOI: **https://doi.org/10.1039/d5mh01287b**.

Acknowledgements

The authors acknowledge Drs. Yu Zhang, Lei Li, and Ying Zhang from the Core Facility of Wuhan University for their assistance with Micro-CT imaging, TEM analysis, and FIB processing. The authors also appreciate the support from the Shiyanjia Lab (**https://www.shiyanjia.com**) for the XPS and DMA characterization studies.

References

1 D. Herzog, V. Seyda, E. Wycisk and C. Emmelmann, Additive manufacturing of metals, *Acta Mater.*, 2016, **117**, 371–392, DOI: **10.1016/j.actamat.2016.07.019**.

2 T. DebRoy, H. L. Wei, J. S. Zuback, T. Mukherjee, J. W. Elmer, J. O. Milewski, A. M. Beese, A. Wilson-Heid, A. De and W. Zhang, Additive manufacturing of metallic components – Process, structure and properties, *Prog. Mater. Sci.*, 2018, **92**, 112–224, DOI: **10.1016/j.pmatsci.2017.10.001**.

3 W. J. Sames, F. A. List, S. Pannala, R. R. Dehoff and S. S. Babu, The metallurgy and processing science of metal additive manufacturing, *Int. Mater. Rev.*, 2016, **61**, 315–360, DOI: **10.1080/09506608.2015.1116649**.

4 L. Johnson, M. Mahmoudi, B. Zhang, R. Seede, X. Huang, J. T. Maier, H. J. Maier, I. Karaman, A. Elwany and R. Arróyave, Assessing printability maps in additive manufacturing of metal alloys, *Acta Mater.*, 2019, **176**, 199–210, DOI: **10.1016/j.actamat.2019.07.005**.

5 H. Hou, E. Simsek, T. Ma, N. S. Johnson, S. Qian, C. Cissé, D. Stasak, N. Al Hasan, L. Zhou, Y. Hwang, R. Radermacher, V. I. Levitas, M. J. Kramer, M. A. Zaeem, A. P. Stebner, R. T. Ott, J. Cui and I. Takeuchi, Fatigue-resistant high-performance elastocaloric materials made by additive manufacturing, *Science*, 2019, **366**, 1116–1121, DOI: **10.1126/science.aax7616**.

6 P. Kürnsteiner, M. B. Wilms, A. Weisheit, B. Gault, E. A. Jägle and D. Raabe, High-strength Damascus steel by additive manufacturing, *Nature*, 2020, **582**, 515–519, DOI: **10.1038/s41586-020-2409-3**.

7 Y. T. Tang, C. Panwisawas, J. N. Ghoussoub, Y. Gong, J. W. G. Clark, A. A. N. Németh, D. G. McCartney and R. C. Reed, Alloys-by-design: Application to new superalloys for additive manufacturing, *Acta Mater.*, 2021, **202**, 417–436, DOI: **10.1016/j.actamat.2020.09.023**.

8 Z. Qu, Z. Zhang, R. Liu, L. Xu, Y. Zhang, X. Li, Z. Zhao, Q. Duan, S. Wang, S. Li, Y. Ma, X. Shao, R. Yang, J. Eckert, R. O. Ritchie and Z. Zhang, High fatigue resistance in a titanium alloy via near-void-free 3D printing, *Nature*, 2024, **626**, 999–1004, DOI: **10.1038/s41586-024-07048-1**.

9 T. M. Pollock, A. J. Clarke and S. S. Babu, Design and Tailoring of Alloys for Additive Manufacturing, *Metall. Mater. Trans. A*, 2020, **51**, 6000–6019, DOI: **10.1007/s11661-020-06009-3**.

10 T. Zhang, Z. Huang, T. Yang, H. Kong, J. Luan, A. Wang, D. Wang, W. Kuo, Y. Wang and C.-T. Liu, In situ design of advanced titanium alloy with concentration modulations by additive manufacturing, *Science*, 2021, **374**, 478–482, DOI: **10.1126/science.abj3770**.

11 T. Song, Z. Chen, X. Cui, S. Lu, H. Chen, H. Wang, T. Dong, B. Qin, K. C. Chan, M. Brandt, X. Liao, S. P. Ringer and M. Qian, Strong and ductile titanium–oxygen–iron alloys by additive manufacturing, *Nature*, 2023, **618**, 63–68, DOI: **10.1038/s41586-023-05952-6**.

12 T. M. Smith, C. A. Kantzos, N. A. Zarkevich, B. J. Harder, M. Heczko, P. R. Gradl, A. C. Thompson, M. J. Mills, T. P. Gabb and J. W. Lawson, A 3D printable alloy designed for extreme environments, *Nature*, 2023, **617**, 513–518, DOI: **10.1038/s41586-023-05893-0**.

13 T. M. Smith, A. C. Thompson, T. P. Gabb, C. L. Bowman and C. A. Kantzos, Efficient production of a high-performance dispersion strengthened, multi-principal element alloy, *Sci. Rep.*, 2020, **10**, 9663, DOI: **10.1038/s41598-020-66436-5**.

14 J. Zhang, M. J. Bermingham, J. Otte, Y. Liu, Z. Hou, N. Yang, Y. Yin, M. Bayat, W. Lin, X. Huang, D. H. StJohn and M. S. Dargusch, Ultrauniform, strong, and ductile 3D-printed titanium alloy through bifunctional alloy design, *Science*, 2024, **383**, 639–645, DOI: **10.1126/science.adj0141**.

15 J. H. Martin, B. D. Yahata, J. M. Hundley, J. A. Mayer, T. A. Schaedler and T. M. Pollock, 3D printing of high-strength aluminium alloys, *Nature*, 2017, **549**, 365–369, DOI: **10.1038/nature23894**.

16 L. Zhou, H. Hyer, S. Park, H. Pan, Y. Bai, K. P. Rice and Y. Sohn, Microstructure and mechanical properties of Zr-modified aluminum alloy 5083 manufactured by laser powder bed fusion, *Addit. Manuf.*, 2019, **28**, 485–496, DOI: **10.1016/j.addma.2019.05.027**.

17 M. Y. Koo, J. S. Park, M. K. Park, K. T. Kim and S. H. Hong, Effect of aspect ratios of in situ formed TiB whiskers on the mechanical properties of TiB_w/Ti–6Al–4V composites, *Scr. Mater.*, 2012, **66**, 487–490, DOI: **10.1016/j.scriptamat.2011.12.024**.

18 Y. Zhu, K. Zhang, Z. Meng, K. Zhang, P. Hodgson, N. Birbilis, M. Weyland, H. L. Fraser, S. C. V. Lim, H. Peng, R. Yang, H. Wang and A. Huang, Ultrastrong nanotwinned titanium alloys through additive manufacturing, *Nat. Mater.*, 2022, **21**, 1258–1262, DOI: **10.1038/s41563-022-01359-2**.

19 J. Yi, L. Wan, T. Shu, X. Zhang, F. Liu and G. J. Cheng, Unleashing multi-scale mechanical enhancement in NiTi shape memory alloy via annular intra-laser deposition with homogenized Ti_2Ni nanoprecipitates, *Acta Mater.*, 2024, **262**, 119418, DOI: **10.1016/j.actamat.2023.119418**.

20 Y. Yang, X. Song, X. Li, Z. Chen, C. Zhou, Q. Zhou and Y. Chen, Recent Progress in Biomimetic Additive Manufacturing Technology: From Materials to Functional Structures, *Adv. Mater.*, 2018, **30**, 1706539, DOI: **10.1002/adma.201706539**.

21 M. Elahinia, N. Shayesteh Moghaddam, M. Taheri Andani, A. Amerinatanzi, B. A. Bimber and R. F. Hamilton, Fabrication of NiTi through additive manufacturing: A review, *Prog. Mater. Sci.*, 2016, **83**, 630–663, DOI: **10.1016/j.pmatsci.2016.08.001**.

22 Y. Chen, M. Klinger, J. Duchoň and P. Šittner, Modulated martensite in NiTi shape memory alloy exposed to high stress at high temperatures, *Acta Mater.*, 2023, **258**, 119250, DOI: **10.1016/j.actamat.2023.119250**.

23 O. Molnárová, M. Klinger, J. Duchoň, H. Seiner and P. Šittner, Plastic deformation of B19' monoclinic martensite in NiTi shape memory alloys: HRTEM analysis of interfaces in martensite variant microstructures, *Acta Mater.*, 2023, **258**, 119242, DOI: 10.1016/j.actamat.2023.119242.

24 G. Li, Y. Huang, X. Li, C. Guo, Q. Zhu and J. Lu, Laser powder bed fusion of nano-titania modified 2219 aluminium alloy with superior mechanical properties at both room and elevated temperatures: The significant impact of solute, *Addit. Manuf.*, 2022, **60**, 103296, DOI: 10.1016/j.addma.2022.103296.

25 T.-C. Lin, C. Cao, M. Sokoluk, L. Jiang, X. Wang, J. M. Schoenung, E. J. Lavernia and X. Li, Aluminum with dispersed nanoparticles by laser additive manufacturing, *Nat. Commun.*, 2019, **10**, 4124, DOI: 10.1038/s41467-019-12047-2.

26 Y. Ma, A. Ahmed, G. Ji, M. Zhang, L. Williams, Z. Chen and V. Ji, Atomic-scale investigation of the interface precipitation in a TiB_2 nanoparticles reinforced Al-Zn-Mg-Cu matrix composite, *Acta Mater.*, 2020, **185**, 287–299, DOI: 10.1016/j.actamat.2019.11.068.

27 M. Farvizi, M. R. Akbarpour, D.-H. Ahn and H. S. Kim, Compressive behavior of NiTi-based composites reinforced with alumina nanoparticles, *J. Alloys Compd.*, 2016, **688**, 803–807, DOI: 10.1016/j.jallcom.2016.06.299.

28 W. Zheng, Y. Shi, L. Zhao, S. Jia, L. Li, C. L. Gan, D. Zhang and Q. Guo, Realizing reversible phase transformation of shape memory ceramics constrained in aluminum, *Nat. Commun.*, 2023, **14**, 7103, DOI: 10.1038/s41467-023-42815-0.

29 R. Cunningham, C. Zhao, N. Parab, C. Kantzos, J. Pauza, K. Fezzaa, T. Sun and A. D. Rollett, Keyhole threshold and morphology in laser melting revealed by ultrahigh-speed x-ray imaging, *Science*, 2019, **363**, 849–852, DOI: 10.1126/science.aav4687.

30 B. N. Sahoo and S. K. Panigrahi, Synthesis, characterization and mechanical properties of in-situ (TiC-TiB_2) reinforced magnesium matrix composite, *Mater. Des.*, 2016, **109**, 300–313, DOI: 10.1016/j.matdes.2016.07.024.

31 H. Kim, H. Choi, J. Oh, S. Lee, H. Kwon, E. S. Park, S. Lee, G.-D. Lee, M. Kim and H. N. Han, Elucidating the role of a unique step-like interfacial structure of η4 precipitates in Al-Zn-Mg alloy, *Sci. Adv.*, 2023, **9**(22), eadf7426, DOI: 10.1126/sciadv.adf7426.

32 Y. Chi, G. Gong, L. Zhao, H. Yu, H. Tian, X. Du and C. Chen, In-situ TiB_2-TiC reinforced Fe-Al composite coating on 6061 aluminum alloy by laser surface modification, *J. Mater. Process. Technol.*, 2021, **294**, 117107, DOI: 10.1016/j.jmatprotec.2021.117107.

33 J. Hu, Q. Yang, S. Zhu, Y. Zhang, D. Yan, K. Gan and Z. Li, Superhard bulk high-entropy carbides with enhanced toughness *via* metastable *in situ* particles, *Nat. Commun.*, 2023, **14**(1), 5157, DOI: 10.1038/s41467-023-41481-6.

34 L. Xun, L. Ying, W. Lu and L. Ruoshan, Ti2Ni and TiNi3 intermetallic compounds to prepare dense TiNi alloy with enhanced recovery property, *Scr. Mater.*, 2023, **234**, 115573, DOI: 10.1016/j.scriptamat.2023.115573.

35 M. Qu, Q. Guo and L. I. Escano, *et al.*, Controlling process instability for defect lean metal additive manufacturing, *Nat. Commun.*, 2022, **13**, 1079, DOI: 10.1038/s41467-022-28649-2.

36 L. Gao, Y. Chen and X. Zhang, *et al.*, Evolution of dislocations during the rapid solidification in additive manufacturing, *Nat. Commun.*, 2025, **16**, 4696, DOI: 10.1038/s41467-025-59988-5.

37 P. Sheng, J. Long and N. Li, *et al.*, Three-dimensional neutron diffraction study of dendrite growth behavior in Ni-based single-crystal turbine blades, *Scr. Mater.*, 2025, **266**, 116770, DOI: 10.1016/j.scriptamat.2025.116770.

38 C. Doñate-Buendia, P. Kürnsteiner, F. Stern, M. B. Wilms, R. Streubel, I. M. Kusoglu, J. Tenkamp, E. Bruder, N. Pirch, S. Barcikowski, K. Durst, J. H. Schleifenbaum, F. Walther, B. Gault and B. Gökce, Microstructure formation and mechanical properties of ODS steels built by laser additive manufacturing of nanoparticle coated iron-chromium powders, *Acta Mater.*, 2021, **206**, 116566, DOI: 10.1016/j.actamat.2020.116566.

39 M.-S. Pham, B. Dovgyy, P. A. Hooper, C. M. Gourlay and A. Piglione, The role of side-branching in microstructure development in laser powder-bed fusion, *Nat. Commun.*, 2020, **11**(749), DOI: 10.1038/s41467-020-14453-3.

40 P. Hua, B. Wang, C. Yu, Y. Han and Q. Sun, Shear-induced amorphization in nanocrystalline NiTi micropillars under large plastic deformation, *Acta Mater.*, 2022, **241**, 118358, DOI: 10.1016/j.actamat.2022.118358.

41 Y. Hu, L. Shu, Q. Yang, W. Guo, P. K. Liaw, K. A. Dahmen and J.-M. Zuo, Dislocation avalanche mechanism in slowly compressed high entropy alloy nanopillars, *Commun. Phys.*, 2018, **1**, 61, DOI: 10.1038/s42005-018-0062-z.

42 P. Chen, X. Cai, Y. Liu, Z. Wang, M. Jin and X. Jin, Combined effects of grain size and training on fatigue resistance of nanocrystalline NiTi shape memory alloy wires, *Int. J. Fatigue*, 2023, **168**, 107461, DOI: 10.1016/j.ijfatigue.2022.107461.

43 J. Cui, Y. S. Chu, O. O. Famodu, Y. Furuya, J. Hattrick-Simpers, R. D. James, A. Ludwig, S. Thienhaus, M. Wuttig, Z. Zhang and I. Takeuchi, Combinatorial search of thermoelastic shape-memory alloys with extremely small hysteresis width, *Nat. Mater.*, 2006, **5**, 286–290, DOI: 10.1038/nmat1593.

44 W. Ni, Y.-T. Cheng, M. J. Lukitsch, A. M. Weiner, L. C. Lev and D. S. Grummon, Effects of the ratio of hardness to Young's modulus on the friction and wear behavior of bilayer coatings, *Appl. Phys. Lett.*, 2004, **85**, 4028–4030, DOI: 10.1063/1.1811377.

45 X. Huang, N. Kang, P. Coddet and M. El Mansori, Analyses of the sliding wear behavior of NiTi shape memory alloys fabricated by laser powder bed fusion based on orthogonal experiments, *Wear*, 2023, **534–535**, 205130, DOI: 10.1016/j.wear.2023.205130.

46 S. Gialanella, G. Ischia and G. Straffelini, Phase composition and wear behavior of NiTi alloys, *J. Mater. Sci.*, 2008, **43**, 1701–1710, DOI: 10.1007/s10853-007-2358-3.

47 R. Li, Time-temperature superposition method for glass transition temperature of plastic materials, *Mater. Sci. Eng., A*, 2000, **278**, 36–45, DOI: 10.1016/S0921-5093(99)00602-4.

48 G. Fan, Y. Zhou, K. Otsuka, X. Ren, K. Nakamura, T. Ohba, T. Suzuki, I. Yoshida and F. Yin, Effects of frequency,

composition, hydrogen and twin boundary density on the internal friction of $Ti_{50}Ni_{50-x}Cu_x$ shape memory alloys, *Acta Mater.*, 2006, **54**, 5221–5229, DOI: 10.1016/j.actamat.2006.06.018.

49 D. Li, W. Liu, N. Li, J. Yan and S. Shi, Remarkable Improvement of Damping Capacity of Mn–20Cu–5Ni–2Fe (at%) Alloy by Zinc Element Addition, *Adv. Eng. Mater.*, 2017, **19**, 1700437, DOI: 10.1002/adem.201700437.

50 S. Zhang, X. Guo, Y. Tang, S. Zhong and Y. Xu, A comparative study on microstructure and damping capacity of Mn-Cu based alloys with dendrite and equiaxial grain, *Vacuum*, 2019, **168**, 108814, DOI: 10.1016/j.vacuum.2019.108814.

51 E. Wang, C. Guo, P. Zhou, C. Lin, X. Han and F. Jiang, Fabrication, mechanical properties and damping capacity of shape memory alloy NiTi fiber-reinforced metal–intermetallic–laminate (SMAFR-MIL) composite, *Mater. Des.*, 2016, **95**, 446–454, DOI: 10.1016/j.matdes.2016.01.130.

52 X. Zhang and L. Wei, Processing and damping capacity of NiTi foams with laminated pore architecture, *J. Mech. Behav. Biomed. Mater.*, 2019, **96**, 108–117, DOI: 10.1016/j.jmbbm.2019.04.036.

53 M. Zhang, Q. Yu, Z. Liu, J. Zhang, G. Tan, D. Jiao, W. Zhu, S. Li, Z. Zhang, R. Yang and R. O. Ritchie, 3D printed Mg-NiTi interpenetrating-phase composites with high strength, damping capacity, and energy absorption efficiency, *Sci. Adv.*, 2020, **6**, eaba5581, DOI: 10.1126/sciadv.aba5581.

54 J. N. Wei, C. L. Gong, H. F. Cheng, Z. C. Zhou, Z. B. Li, J. P. Shui and F. S. Han, Low-frequency damping behavior of foamed commercially pure aluminum, *Mater. Sci. Eng., A*, 2002, **332**, 375–381, DOI: 10.1016/S0921-5093(01)01950-5.

55 J. H. Zhang, W. Y. Peng, J. J. Zhang and Z. Xu, Shape memory effect of an antiferromagnetic Mn–9.5at% Fe–5.0at% Cu alloy, *Mater. Sci. Eng., A*, 2008, **481–482**, 326–329, DOI: 10.1016/j.msea.2006.12.222.

56 Y. Song, M. Jin, X. Han, X. Wang, P. Chen and X. Jin, Microstructural origin of ultrahigh damping capacity in Ni50.8Ti49.2 alloy containing nanodomains induced by insufficient annealing and low-temperature aging, *Acta Mater.*, 2021, **205**, 116541, DOI: 10.1016/j.actamat.2020.116541.

57 S. Li, H. Hassanin, M. M. Attallah, N. J. E. Adkins and K. Essa, The development of TiNi-based negative Poisson's ratio structure using selective laser melting, *Acta Mater.*, 2016, **105**, 75–83, DOI: 10.1016/j.actamat.2015.12.017.

58 L.-Y. Chen, S.-X. Liang, Y. Liu and L.-C. Zhang, Additive manufacturing of metallic lattice structures: Unconstrained design, accurate fabrication, fascinated performances, and challenges, *Mater. Sci. Eng., R*, 2021, **146**, 100648, DOI: 10.1016/j.mser.2021.100648.

59 H. Sehitoglu, I. Karaman, R. Anderson, X. Zhang, K. Gall, H. J. Maier and Y. Chumlyakov, Compressive response of NiTi single crystals, *Acta Mater.*, 2000, **48**, 3311–3326, DOI: 10.1016/S1359-6454(00)00153-1.

60 S. Saedi, N. Shayesteh Moghaddam, A. Amerinatanzi, M. Elahinia and H. E. Karaca, On the effects of selective laser melting process parameters on microstructure and thermomechanical response of Ni-rich NiTi, *Acta Mater.*, 2018, **144**, 552–560, DOI: 10.1016/j.actamat.2017.10.072.

61 P. Hua, K. Chu, F. Ren and Q. Sun, Cyclic phase transformation behavior of nanocrystalline NiTi at microscale, *Acta Mater.*, 2020, **185**, 507–517, DOI: 10.1016/j.actamat.2019.12.019.

62 Z. C. Eckel, C. Zhou, J. H. Martin, A. J. Jacobsen, W. B. Carter and T. A. Schaedler, Additive manufacturing of polymer-derived ceramics, *Science*, 2016, **351**, 58–62, DOI: 10.1126/science.aad2688.

63 Y. Wang, X. Zhang, Z. Li, H. Gao and X. Li, Achieving the theoretical limit of strength in shell-based carbon nanolattices, *Proc. Natl. Acad. Sci. U. S. A.*, 2022, **119**, e2119536119, DOI: 10.1073/pnas.2119536119.

64 B. Deng, R. Xu, K. Zhao, Y. Lu, S. Ganguli and G. J. Cheng, Composite bending-dominated hollow nanolattices: A stiff, cyclable mechanical metamaterial, *Mater. Today*, 2018, **21**, 467–474, DOI: 10.1016/j.mattod.2018.03.027.

65 L. C. Montemayor and J. R. Greer, Mechanical Response of Hollow Metallic Nanolattices: Combining Structural and Material Size Effects, *J. Appl. Mech.*, 2015, **82**(7), 071012, DOI: 10.1115/1.4030361.

66 M. Mieszala, M. Hasegawa, G. Guillonneau, J. Bauer, R. Raghavan, C. Frantz, O. Kraft, S. Mischler, J. Michler and L. Philippe, Micromechanics of Amorphous Metal/Polymer Hybrid Structures with 3D Cellular Architectures: Size Effects, Buckling Behavior, and Energy Absorption Capability, *Small*, 2017, **13**, 1602514, DOI: 10.1002/smll.201602514.